Neural population dynamics during sleep in a songbird vocal circuit resemble sharp wave ripple activity

Corinna Lorenz[1,2]*, Anindita Das[2]*, Eduarda Gervini Zampieri Centeno[3,5]*, Hamed Yeganegi[4,6], Robin Duvoisin[1], Roman Ursu[3], Aude Retailleau[3], Nicolas Giret[2], Arthur Leblois[3], Richard H. R. Hahnloser[1], and Janie M. Ondracek[4]†

[1] Institute of Neuroinformatics, University of Zurich and ETH Zurich, 8057, Zurich, Switzerland
[2] Institut des Neurosciences Paris-Saclay, CNRS, 151 route de la rotonde, 91400 Saclay, France
[3] Bordeaux Neurocampus, Institut des Maladies Neurodégénératives, 146 rue Léo-Saignat - 33076 Bordeaux Cedex
[4] Technical University of Munich, TUM School of Life Sciences, Chair of Zoology, Liesel-Beckmann-Straße 4, 85354 Freising, Germany
[5] Amsterdam UMC location Vrije Universiteit Amsterdam, Anatomy and Neurosciences, De Boelelaan 1117, Amsterdam, The Netherlands
[6] Graduate School of Systemic Neurosciences, Ludwig-Maximilians-University Munich, Großhaderner Str. 2, 82152, Planegg, Germany
(*) Authors contributed equally
(†) Corresponding author

Current email address:
corinna@ini.ethz.ch
anindita.das@cnrs.fr
egervinizamp@u-bordeaux.fr
hamed.yeganegi@tum.de
rduvoisin@ethz.ch
ursu@bio.ens.psl.eu
aude.retailleau@u-bordeaux.fr
nicolas.giret@universite-paris-saclay.fr
arthur.leblois@u-bordeaux.fr
rich@ini.ethz.ch
janie.ondracek@tum.de

Abstract

During vocal learning, juvenile songbirds use auditory feedback and trial-and-error motor learning to transition from acoustically simple, highly variable songs to complex and stereotypical adult songs. Similar to motor skill learning in mammals, vocal learning in songbirds requires a set of interconnected brain areas that make up an analogous basal ganglia-thalamocortical circuit known as the anterior forebrain pathway (AFP). Although neural

activity in the AFP has been extensively investigated during awake singing, very little is known about its neural activity patterns during offline sleep periods.

In this work, we used chronically implanted Neuropixels probes to investigate neural activity in the AFP during offline periods of natural sleep. We found that neurons in the pallial region LMAN (lateral magnocellular nucleus of the nidopallium) transitioned from sparse synchronous firing to asynchronous firing during sleep, which corresponded to slow wave sleep (SWS) and rapid eye movement (REM) sleep, respectively. SWS periods were associated with increased spiking variability for LMAN neurons, but not for neurons in the striatal region Area X (proper name). Coinciding with the increased spiking variability, we observed that populations of LMAN neurons were co-activated at specific time points during sleep in bursting events that were characterized by a negative deflection in the local field potential (LFP) and a transient increase in gamma power. Overall, the LMAN population bursting events were highly reminiscent of sharp-wave ripple (SWR) activity observed in rodent hippocampus.

Contrary to our expectations, we did not observe strong cross-area field coherence between LMAN and Area X, although individual LMAN-Area X LFP pairs did show coherence > 0.5. These results provide the first description of cross-area dynamics within the AFP during sleep. Furthermore, the observation of SWR-like events during sleep in LMAN suggests that large-scale population events have diverse functions across vertebrates.

Introduction

Cortical and basal ganglia (BG) circuits regulate behavioral variability, as evidenced by studies of habit and skill learning in mammals (Graybiel, 2008; Knowlton et al., 1996; Santos et al., 2015; Wise et al., 1996; Yin et al., 2009). Acquiring novel skills usually first requires exploration of the behavioral space (Grunow & Neuringer, 2002; Kao et al., 2005; Olveczky et al., 2005; Tumer & Brainard, 2007; Wu et al., 2014). Then, through a process of learning, behavioral variability is reduced and the relevant behavioral output is refined. This refinement is usually accompanied by a decrease in neuronal variability. In rodents, for examples, the production of skilled motor actions coincides with the emergence of coordinated neural activity across the motor cortex and striatum (Koralek et al., 2013; Lemke et al., 2021; Santos et al., 2015).

Vocal learning in songbirds is an innate motor learning skill that has been investigated for decades (Konishi, 1965, 1970; McCasland & Konishi, 1981). A juvenile bird learns to sing through a complex sensorimotor process that involves the formation of auditory memories of the target song, sequences of motor output, and associative higher-order representations of learned vocalizations to transition from acoustically simple, highly variable “subsongs” to complex and stereotypical adult songs (Kollmorgen et al., 2020; Margoliash & Schmidt, 2010). Critically involved in this learning process is a set of interconnected brain areas that make up a basal ganglia-thalamocortical circuit (Fig. 1A) known as the AFP (Andalman & Fee, 2009; Bottjer et al., 1984; Brainard & Doupe, 2000; Farries & Perkel, 2002; Scharff & Nottebohm, 1991).

Within the AFP, the pallial structure LMAN exerts a direct influence on vocal output through its projection to premotor area RA (robust nucleus of the arcopallium), presumably modulating downstream neural activity through bursts of spikes (Kao et al., 2008; Kojima et al., 2013;

Palmer et al., 2021). Through this influence, LMAN drives behavioral variability that can be used for learning (Tumer & Brainard, 2007). Area X, part of the avian striatum (Person et al., 2008; Pfenning et al., 2014), is thought to receive an efference copy of activity in LMAN (Andalman & Fee, 2009; Vates et al., 1997; Vates & Nottebohm, 1995), thus placing Area X in a position to evaluate LMAN exploratory activity in the context of the ongoing song via a dopaminergic reward signal (Duffy et al., 2022; Gadagkar et al., 2016).

While it is clear that cortico(pallial)-striatal circuits are required for learning in both birds (Ali et al., 2013; Andalman & Fee, 2009; Bottjer et al., 1984; Olveczky et al., 2005; Scharff & Nottebohm, 1991; Tumer & Brainard, 2007; Zai et al., 2020) and mammals (Kawai et al., 2015; Lemke et al., 2021; Santos et al., 2015), including humans (Debas et al., 2014), little is known about the specific activity patterns that drive learning, or when they occur.

One intriguing possibility is that neural activity patterns that occur during 'offline' periods such as sleep may be critically involved in learning. Substantial evidence in rodents has shown that 'reactivations' of training-related neural activity patterns during sleep accompany motor skill learning (Gulati et al., 2014; Lemke et al., 2021; Ramanathan et al., 2015). While similar reactivations occur during sleep in songbirds (Elmaleh et al., 2021, 2023; Shank & Margoliash, 2009; Young et al., 2017), their specific role in learning remains unclear. And although sleep has a clear effect on the vocal output of juvenile birds engaged in vocal learning (Derégnaucourt et al., 2005; Kollmorgen et al., 2020) as well as the neural activity of brain areas involved in awake song production (Dave & Margoliash, 2000; Elmaleh et al., 2021; Hahnloser & Fee, 2007), the neural activity patterns during sleep in the AFP are largely unexplored (although see (Yanagihara & Hessler, 2012).

Zebra finches (*Taeniopygia guttata*) share many features of sleep with mammals, including transitions through SWS and REM sleep (Low et al., 2008; Yeganegi & Ondracek, 2023). Additionally, birds show an intermediate stage (IS) of sleep, which has been compared to the early stages of mammalian non-REM (NREM) sleep and which can be considered a transitional stage of sleep. Importantly, sleep spindles, a hallmark of mammalian NREM, have not been observed during avian sleep (Canavan & Margoliash, 2020; Low et al., 2008).

We used a new approach (Lorenz, 2024) to chronically implant Neuropixels1.0 probes (Jun et al., 2017) to investigate neural dynamics in the pallial-striatal network during natural sleep in seven male zebra finches. Although we did not study brain dynamics during times when the animals were actively engaged in a learning paradigm, parallels between sleep characteristics previously identified in mammals and existing parallels in songbirds could hint towards convergent strategies within the cortico-striatal pathway.

Results

Distinct regimes of activity are present during avian sleep

We investigated neural activity during sleep in the pallium and basal ganglia of male zebra finches (n = 7) chronically implanted with Neuropixels 1.0 probes (Fig. 1B). In each animal, the probe was implanted such that both the pallial structure LMAN and the striatal structure Area X within the avian BG (Person et al., 2008) were targeted (Fig. 1C).

We observed that during sleep, slow wave delta activity (1-4 Hz) in the local field potential (LFP) was widespread throughout the pallium and BG, spanning more than 4 mm (Fig. 1D). Neural spiking was synchronized with the slow wave dynamics and was observable as sparsely bursting patterns of activity in both pallial and BG neurons (Figure 1D). In contrast to these periods of synchronized bursting, we also observed short periods of asynchronous firing (Fig. 1D-E, black box).

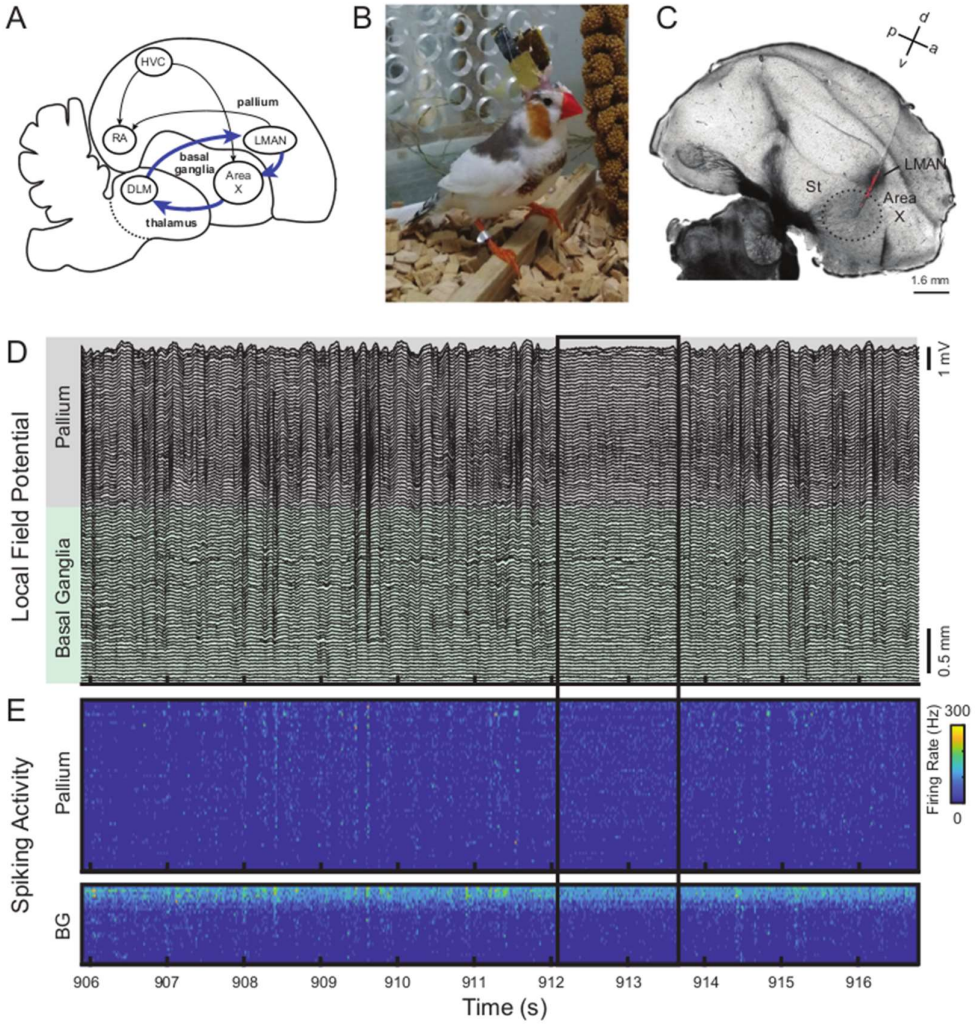

Figure 1: Pallial-basal ganglia dynamics during sleep in a songbird. (A) Schematic depicts the basal ganglia-thalamocortical circuit (blue arrows). Black arrows indicate other important connections of the song system. HVC, proper name; RA, robust nucleus of the arcopallium; LMAN, lateral magnocellular nucleus of the nidopallium; Area X, proper name; DLM, medial dorsolateral nucleus of the thalamus. **(B)** Image of a male zebra finch implanted with a Neuropixels1.0 probe. **(C)** Histological brain slice depicting the Neuropixels electrode track (red DiI fluorescence). Area X is indicated with a dotted black line. St, striatum; d, dorsal; a, anterior; v, ventral; p, posterior; for other abbreviations, see (A). Histology from ZF-2. **(D)** 10 s segment of local field potentials (LFP) recorded during sleep in ZF-1. Recording sites were located in the pallium (gray shading) and basal ganglia (green shading) and are organized according to depth. **(E)** Corresponding spiking activity for identified pallial or striatal neurons. Firing rate is indicated with the color scale, and neurons are sorted according to firing rate. Note how neural activity transitions from sparse and synchronous firing aligned to the LFP troughs to asynchronous firing at 912-914 s (black box).

We hypothesized that these two regimes corresponded to SWS and REM sleep states. We used two complementary approaches to further clarify these activity states: 1) we analyzed sleep as a continuous variable using the LFP δ/γ power ratio, and 2) we categorized sleep into discrete stages using an automated avian sleep clustering algorithm (Canavan & Margoliash, 2020; Low et al., 2008). Whereas the former approach acknowledges the continuous nature of sleeping brain dynamics, the latter approach allowed us to numerically characterize certain aspects of avian sleep and compare our results with other avian sleep studies.

Using the first method, we calculated the δ/γ ratio as the ratio of delta activity (δ, 1-4 Hz) to gamma activity (γ, 30-90 Hz). This method is analogous to metrics that have been used with rodents (Csicsvari et al., 1998; O'Keefe, 1976; Siapas & Wilson, 1998), but accounts for the dominant frequency bands present during avian sleep (Low et al., 2008; Yeganegi et al., 2019; Yeganegi & Ondracek, 2023).

We calculated the δ/γ ratio for a large range of pallial and BG sites (Fig. 2A). Whereas δ/γ ratios calculated for LFPs within the BG were mostly flat, δ/γ ratios calculated for pallial LFPs were large and dynamic (Fig. 2A, black line). LPF traces with low δ/γ values corresponded to putative REM states (e.g., low amplitude LFP signals), while LPF traces with high δ/γ corresponded to putative SWS states (e.g., large amplitude LFP signals; Fig. 2B). Median δ/γ values, calculated using a centrally located pallial LFP for each bird individually, showed some variability across birds (Fig. 2C) but were within the range of values previously reported using similar metrics (Yeganegi & Ondracek, 2023).

We used a clustering-based sleep scoring method (Canavan & Margoliash, 2020; Low et al., 2008) to confirm sleep stages, and we observed that sleep-scored SWS segments were indeed characterized by high δ/γ values, and REM sleep segments were characterized by low δ/γ values, with IS states falling in between the two distributions (Fig. 2D-F). 3-D plots showed that sleep states were well-segregated on the basis of the spectral features used in the clustering-based approach (Figure 2G, H; Figure 2 Supplement 1).

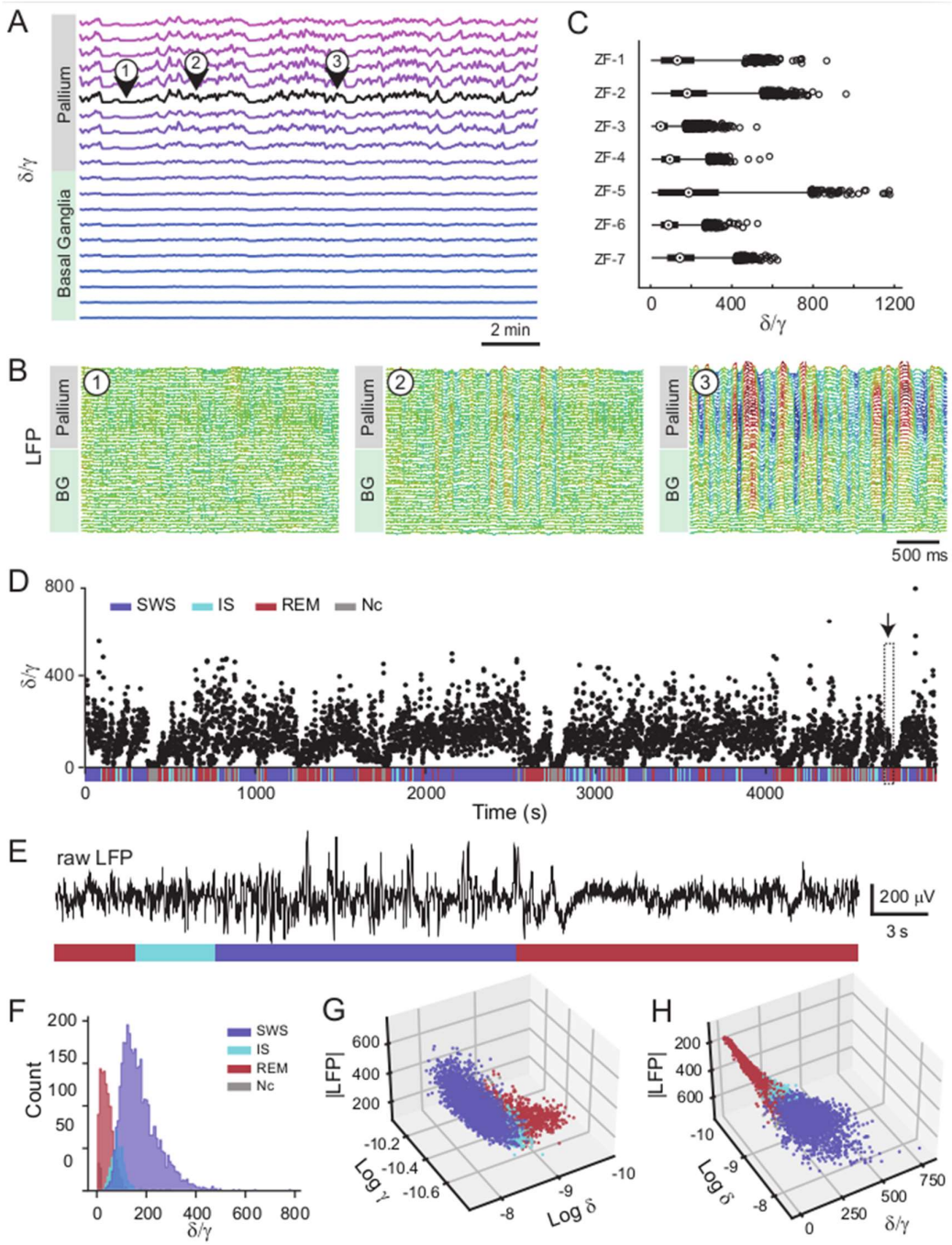

Figure 2: Identification of sleep stages and representative neural dynamics. (A) Ratio of δ/γ power for consecutive depths along the Neuropixels shank. Each trace is separated by 200 um. Black trace indicates the δ/γ trace calculated for a centrally located pallial LFP. Numbers and arrows indicate low (1), middle (2), and high (3) δ/γ values. δ/γ values calculated for a 3-s LFP window, as depicted in (B). Data from ZF-1. **(B)** 3-second segments of local field potential (LFP) activity from pallial and BG sites for the low, middle, and high δ/γ values indicated in (A). Each trace is separated by 80 um. Note the large amplitude slow wave dynamics present for high δ/γ values indicated in (3). Linear color scale for visualization purposes only. Data from ZF-1. **(C)** Bar plots indicate average δ/γ values calculated in 3-s windows for the duration of the sleep phase per bird. The box bottom and top edges represent the 25th and 75th percentile, respectively, and the middle dot represents the median. Whisker extends to the 25-75 percentile, and outliers beyond this range are indicated as open circles. **(D)** δ/γ values for an entire recording duration for an example bird (ZF-7) plotted with the identified sleep stages as colored bars below. SWS, slow wave sleep; IS, intermediate sleep; REM, rapid eye-movement sleep; Nc, not categorized. Dotted black box indicated with the black arrow is enlarged in (E). **(E)** 30 s trace of raw LFP from the pallial site used for sleep staging

(see Methods for details). Color-coded bars indicate classified sleep stages. Note how SWS segments correspond to a large amplitude LFP signal and REM segments correspond to a low amplitude LFP signal. **(F)** Histogram of δ/γ values grouped according to identified sleep states. Note how SWS segments correspond to high δ/γ values and REM segments correspond to low δ/γ values. Same bird as in (D). See Figure 2 Supplement 1 for data from other birds. **(G, H)** Plots show that sleep state clusters are segregated in 3-D space according to the features used for classification, e.g., mean LFP magnitude, the delta (δ) and gamma (γ) power, δ/γ values. Each dot represents a 1-s snippet of sleeping data (resolution of the automated sleep staging procedure). Same bird as in (D).

Different spectral features characterize sleep and awake states

Were the activity patterns that we observed during sleep different than those observed during wakefulness? We compared the spectral features of LFP signals recorded in LMAN and Area X during awake and sleep phases in three birds (Fig. 3A, B). We observed that in LMAN, the power was higher for a broad range of low frequencies during sleep compared to awake states (e.g., 1-30 Hz; Fig. 3B, asterisks). In contrast, for LFPs recorded within Area X, only the power in the theta range (4-12 Hz) was higher during sleep compared to awake states.

The power in the high-frequency gamma range (90-145 Hz) was higher for LMAN LFPs during awake states compared to sleep states (Fig. 3B, asterisks), but this was not the case for LFPs in Area X, which were similar for awake and sleep states.

In general, we saw that sleep states were associated with higher power in low frequency bands compared to awake states (Fig. 3C), which is in line with results from brain areas including RA (Hahnloser et al., 2006) and Area X (Yanagihara & Hessler, 2012). Importantly, the depth associated with LMAN LFPs (Fig. 3C, thick orange line; 2600 um) was strongly modulated by sleep. We saw that LFPs at the deepest part of the probe followed the common 1/f power spectrum but generally carried less power (Fig. 3C, black lines: 100 um from probe tip).

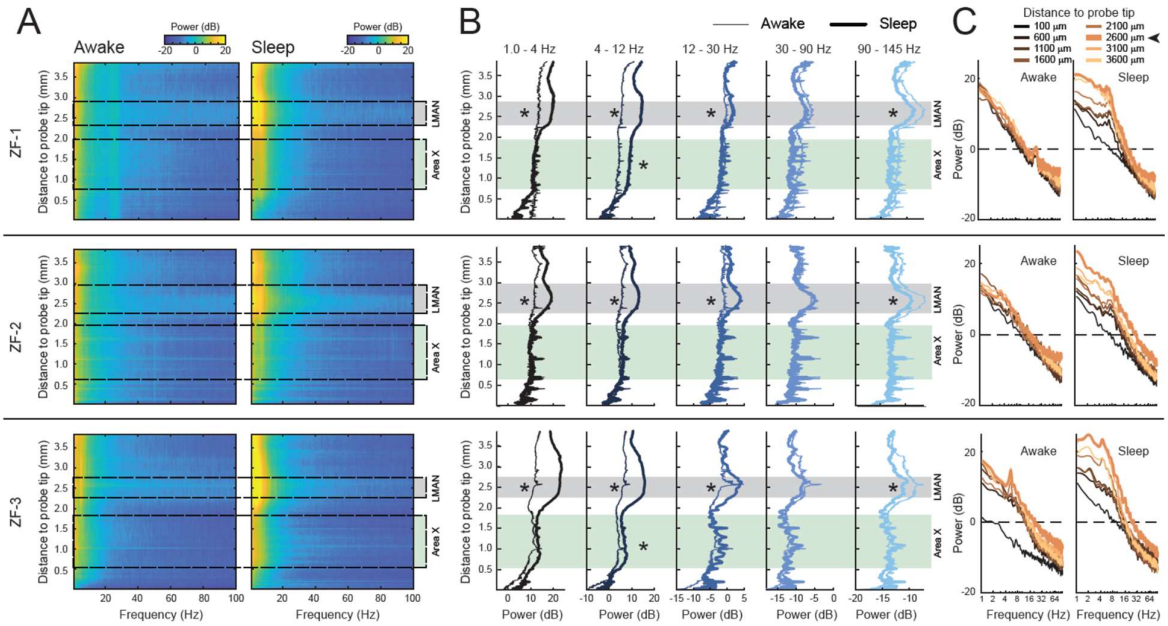

Figure 3: Sleep-related modulation of low-frequency power is higher in pallium compared to the striatum (**A**) The color-coded power spectrum density (PSD) of the LFP signal for each electrode is displayed, organized by depth (dorsal to ventral), for both the awake state (left) and sleep state (right) across 3 birds (top to bottom). Warm color indicates high power, cool colors indicate low power. The electrode depths corresponding to LMAN (gray box, dashed line) and Area X (green box, dashed line) are indicated for each bird. The analysis is based on the average

PSD derived from 10 randomly selected 10-sec windows. **(B)** Power distribution across electrode sites provide a detailed comparison between awake (thin lines) and sleep (thick lines) for different frequency bands. LMAN exhibits higher gamma band power (90-145 Hz) during awake states compared to sleep states (LMAN; black asterisks). In contrast LMAN exhibits higher power in low frequency bands (1-30 Hz) during sleep compared to awake states (LMAN; black asterisks). A difference in sleep and awake states in Area X is largely absent, with the exception of the theta band power (4-12 Hz), which showed a slight increase in two birds during sleep (Area X; black asterisks). **(C)** The marginal distribution of power across depths is displayed for awake and sleep states for each bird. Note that the distances in the legend refer to the distance from the probe tip, (i.e., 100 um from the probe tip). Thick orange line indicates depth associated with LMAN (i.e., 2600 um, black arrowhead); note how it is strongly modulated by sleep. Dotted line indicates 0 dB.

Pallial-basal ganglia LFP exhibit high spatially widespread intra-areal coherence during slow wave sleep

Given the clear spectral differences that we observed between LMAN and Area X during sleep and awake states, we focused our next analysis on investigating the functional connectivity between these brain areas.

We characterized the intra-area LFP coherence within LMAN and within Area X (Fig. 4A-C) as well as across LMAN and Area X (Fig. 4D) averaged across all birds. We calculated the magnitude squared coherence between all pairs of LMAN and Area X electrodes for 6-s long REM sleep and SWS segments (Fig. 4 Supplement 1), for different canonical frequency ranges that have been shown to play an important role in behavior (Buzsáki & Draguhn, 2004).

We observed the average pairwise LFP coherence across birds to be significantly modulated by sleep states (Fig. 4E-G, Fig. 4 Supplement 2 and 3). During SWS, we observed very high intra-area coherence values for the delta band for pairs of LMAN LFPs, ranging from 0.69 - 0.99 (min - max, median = 0.94; Table 1). During REM sleep, the median pairwise coherence value for the delta band was still high for LMAN LFP pairs (median = 0.83), but the range of values was larger (0.307 - 0.99; min - max), indicating a decrease in coherence between LMAN pairs during REM sleep.

Similar to LMAN pairs, median coherence values were lower for REM sleep compared to SWS for all Area X LFP pairs; however, pairwise LFP coherence within Area X was generally lower compared to LMAN pairs for all frequency ranges (Table 1). This finding is consistent with primate literature demonstrating significantly lower coherence within basal ganglia compared to cortical areas during SWS (Mizrahi-Kliger et al., 2018).

LMAN sends direct projections to Area X, which in turn sends feedback projections to LMAN through thalamic area DLM (Fig. 1A; (Farries et al., 2005). If the closed-loop structure of the circuit plays an important role in modulating sleep dynamics, we may expect strong cross-area coherence.

While median coherence values were low across frequency bands for LMAN-Area X LFP pairs compared to intra-LMAN or intra-Area X LFP pairs (Table 1), individual LMAN-Area X LFP pairs showed high coherence values > 0.5, especially for the low frequencies (1-30 Hz; Fig. 4G; see also Fig. 4 supplement 3, blue dots). This finding shows that individual pairs of LMAN - Area X LFP shared similar oscillatory drive during sleep.

We did not find strong modulation in the coherence for LMAN-Area X LFP pairs as a function of sleep state: although many frequency bands were statistically different (Fig. 4G), the median differences were quite small (Table 1).

We did not observe a large effect of sleep state on coherence as a function of spatial distance (Fig. 4 H-M). Whereas coherence in the low frequency ranges was spatially widespread during SWS (Fig. 4H-J), coherence in the gamma frequency bands were limited to spatially neighboring channels with the coherence values dropping to 50% of its peak value within 150 microns. This is consistent with the idea that gamma oscillations reflect local network dynamics (Buzsáki & Wang, 2012; Cardin, 2016; Cardin et al., 2009).

Brain Area	Frequency range	SWS: Median coherence (Min, Max values)	REM: Median coherence (Min, Max values)	Wilcoxon signed rank test (p value)
LMAN	**Delta**: 1 – 4 Hz	**0.942** (0.693, 0.996)	**0.828** (0.307, 0.987)	7.94E-75
	Theta: 4 – 12 Hz	**0.944** (0.741, 0.995)	**0.838** (0.479, 0.986)	4.11E-76
	Beta: 12 – 30 Hz	**0.751** (0.191, 0.961)	**0.608** (0.191, 0.961)	6.00E-76
	Low gamma: 30 – 90 Hz	**0.345** (0.056, 0.848)	**0.309** (0.052, 0.860)	2.73E-35
	High gamma: 90 – 140 Hz	**0.230** (0.028, 0.764)	**0.222** (0.022, 0.806)	0.134
Area X	**Delta**: 1 – 4 Hz	**0.561** (0.006, 0.955)	**0.366** (0.006, 0.876)	0
	Theta: 4 – 12 Hz	**0.649** (0.044, 0.981)	**0.516** (0.055, 0.935)	0
	Beta: 12 – 30 Hz	**0.371** (0.026, 0.909)	**0.264** (0.020, 0.909)	0
	Low gamma: 30 – 90 Hz	**0.174** (0.022, 0.767)	**0.162** (0.0197, 0.699)	6.69E-292
	High gamma: 90 – 140 Hz	**0.132** (0.021, 0.703)	**0.128** (0.0178, 0.649)	1.12E-97
LMAN - X	**Delta**: 1 – 4 Hz	**0.172** (0.001, 0.924)	**0.177** (0.003, 0.846)	4.64E-16
	Theta: 4 – 12 Hz	**0.295** (0.011, 0.919)	**0.254** (0.010, 0.823)	9.10E-69
	Beta: 12 – 30 Hz	**0.129** (0.006, 0.615)	**0.120** (0.005, 0.607)	2.80E-04
	Low gamma: 30 – 90 Hz	**0.074** (0.013, 0.274)	**0.076** (0.014, 0.272)	0.325
	High gamma: 90 – 140 Hz	**0.059** (0.016, 0.248)	**0.045** (0.012, 0.207)	1.83E-306

Table 1: Average coherence values for all birds (n = 7) used for analysis in Fig 4.

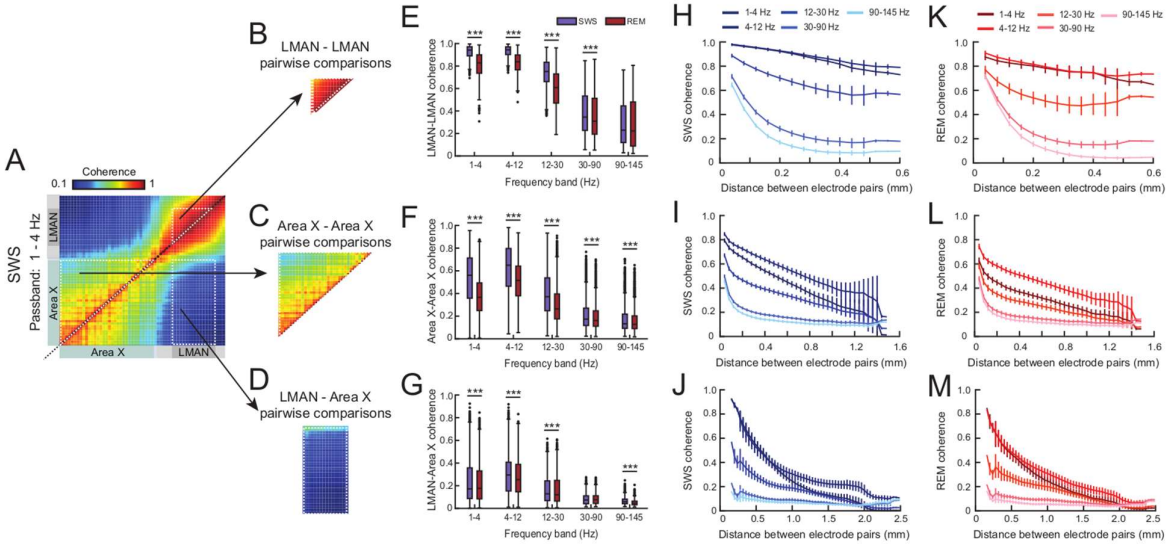

Figure 4: LFP coherence in the pallial-striatal circuit is modulated by sleep states. (A) Heat map represents a color-coded representation of the average pairwise coherence calculated for the 1-4 Hz passband for all SWS segments. Warm colors indicate high coherence values, and cool colors indicate low coherence values. The diagonal black dotted line indicates symmetry. The white dotted triangles along the line of symmetry indicate the pallial electrode sites that were included in the LMAN-LMAN coherency analysis (corresponding to the gray LMAN shading) or the BG electrode sites that were included in the Area X-Area X coherence analysis (green Area X shading). The white dotted rectangle (lower right quadrant) indicates the sites that were included in the LMAN-Area X coherency analysis. (B-D) Visual representation of the electrode site comparisons that were used in the coherency analysis. **(B)** LMAN-LMAN comparisons. **(C)** Area X- Area X comparisons. **(D)** LMAN-Area X comparisons. **(E-G)** Box plots indicate the median coherency values across different frequency bands for LMAN-LMAN comparisons (**E**), Area X-Area X comparisons **(F)**, and LMAN-Area X comparisons **(G)**. Blue boxes indicate SWS, red boxes indicate REM sleep. The box bottom and top edges represent the 25th and 75th percentile, respectively, and the middle line represents the median. Whisker extends to the 25-75 percentile, and outliers beyond this range are indicated as circles. Asterisks indicate significance (Wilcoxon sign rank test; ***$p \leq 0.001$). **(H-J)** Panels indicate the change in SWS coherence as a function of inter-electrode distance for **(H)** Inter-area LMAN - LMAN comparisons, **(I)** Inter-area Area X - Area X comparisons, and **(J)** Cross-area LMAN - Area X comparisons. Different colored lines indicate different frequency bands. Error bars indicate the iqr. (K-M) Panels indicate the change in REM sleep coherence as a function of inter-electrode distance. **(K)** Inter-area LMAN - LMAN comparisons. **(L)** Inter-area Area X - Area X comparisons. **(M)** Cross area LMAN - Area X comparisons.

Phases of high δ/γ activity during sleep area associated with increased spiking variability for neurons in LMAN but not Area X

Using our Neuropixels recordings, we leveraged the high-pass filtered electrode signals to investigate the spiking activity in LMAN and Area X during sleep in n = 5 birds. Spikes were identified and assigned using state-of-the-art automatic detection and sorting algorithms, either in a fully automated way or followed by meticulous manual curation to ensure accuracy and reliability (see Methods). The results of any spiking analysis did not differ qualitatively across these two preprocessing approaches.

During sleep, we observed increased but sparse population-wide spiking activity which was locked to slow wave LFP troughs and interleaved with periods of neural silence, followed by sudden switches to periods of random spiking and lower LFP amplitudes (see Fig. 1D-E). To quantify the different patterns of spiking activity that we observed during sleep, we calculated

the coefficient of variation (CV, standard deviation divided by the mean) for identified LMAN and Area X neuron populations in 10 ms bins during sleep (Fig. 5A). We found that median CVs ranged from 0.27 in Area X to 1.69 in LMAN (see Table 2 for individual values), and CV values were significantly higher for LMAN neurons compared to Area X neurons in all birds (median LMAN CV over all birds = 1.44 ± 0.21 (s.e.m.); median Area X CV for all birds was = 0.61 ± 0.14).

We observed that the CV values fluctuated closely with δ/γ values, such that high CV values were associated with high δ/γ values (Fig. 5B). This trend was especially obvious for LMAN neurons (Figure 5C, Fig. 5 Supplement 1). Indeed, we found that CV values for LMAN neurons were highly correlated with δ/γ values for all birds (Fig. 5D, Fig. 5 Supplement 1; Table 3). This was not the case for Area X neurons: 2/5 birds showed significant positive correlations between CV values and δ/γ values, whereas 1 bird showed a significant negative correlation (Table 3).

The CV can be thought of as a measure of collective variability in coincident spike trains: CV values for the population rate will approach zero when all neurons are statistically independent (Kobak et al., 2019). This is because random irregularities stemming from individual neurons will average out as the population size increases, ultimately leading to a stable population rate. However, when neurons are synchronized and activity oscillates, the variability from one moment to another in the population rate is high.

High CV values for LMAN neurons compared to lower CV values for Area X neurons (Fig. 5A) suggest that the spike trains for LMAN neurons were more irregular than for Area X neurons. Indeed, when we examined spike rasters corresponding to high CV values for LMAN populations (Fig. 5E), spiking patterns were conspicuously irregular - albeit largely synchronized as bursts of spikes across the population of LMAN neurons. In contrast, CV values were significantly lower for Area X neurons (Fig. 5A), capturing their regular spiking patterns and high firing rates (Fig. 5E).

It is important to note that the δ/γ trace used in this analysis was calculated from a centrally located LMAN LFP (see Methods for details). Therefore, strong correlations between CV values and δ/γ values in LMAN may reflect the tight correspondence between spiking activity and LFP oscillations in LMAN. The correspondence between spiking activity in Area X and LMAN LFP was much more heterogeneous, suggesting that oscillatory activity in LMAN did not directly influence Area X spiking activity during sleep as it did in LMAN.

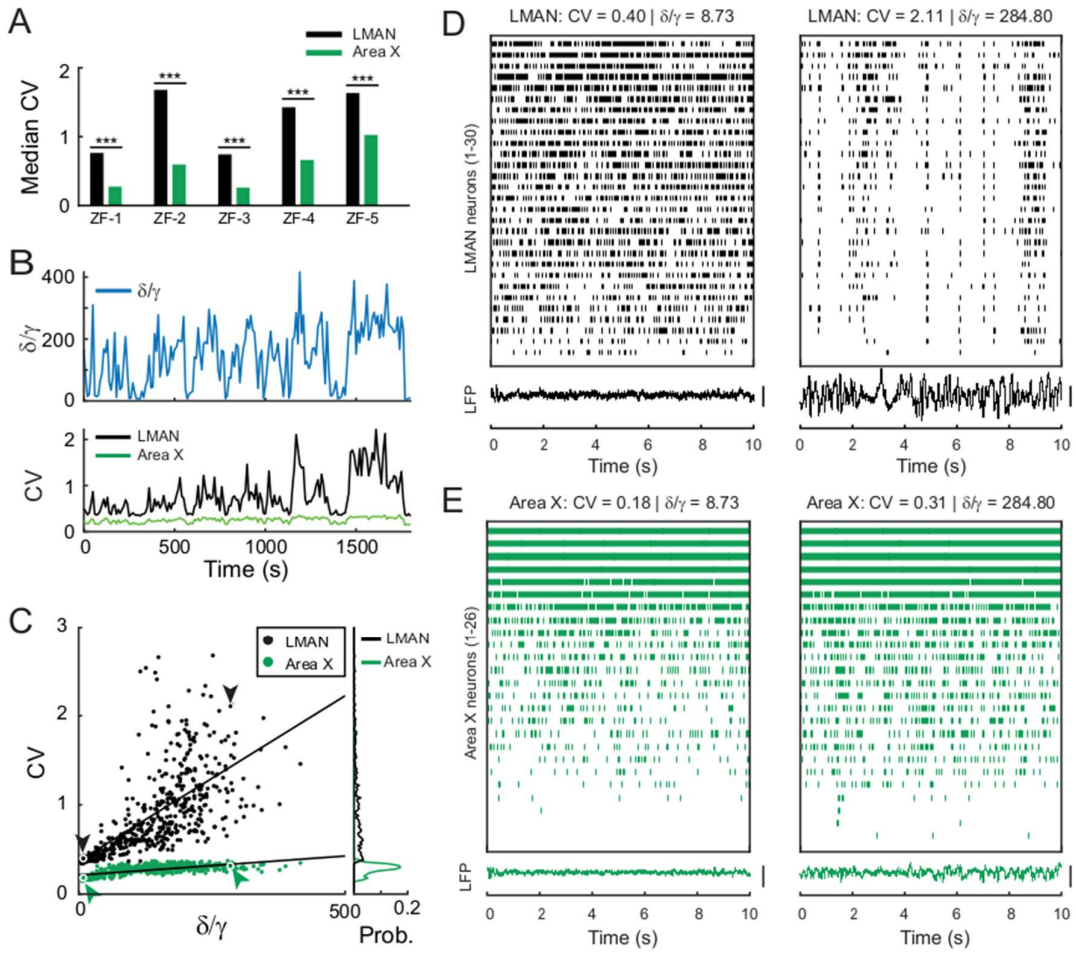

Figure 5: Spiking variability is significantly higher for LMAN neurons compared to Area X neurons. (A) Bar plots summarize CV values for 7 finches (black bars, LMAN population; green bar, Area X population). CV values were higher for LMAN populations compared to Area X populations. **(B)** δ/γ values (top, blue line) were highly correlated with CV values (bottom) for both LMAN and Area X populations. δ/γ values and CV values computed in 10 s windows. **(C)** Scatter plot indicates the CV versus δ/γ values for ZF-1. LMAN, black dots; Area X, green dots. Black and green arrows indicate the data points that correspond to the 10 s snippet of data plotted in (D) and (E). The marginal distributions for the CV values are plotted (right) for LMAN (black line) and Area X neurons (green line). See Figure 5 Supplement 1 for data from other birds. **(D)** Spiking raster plot for 33 LMAN neurons for an example time window with low CV value (left plot) and a high CV value (right box). Each tick corresponds to a spike and neurons are sorted by their average spiking activity from high (top) to low (bottom). Corresponding 10 s LFP trace is plotted at the bottom of the raster plot. Vertical bar is 500 uV. Data correspond to black arrows in (C). (**E)** Spiking raster plot for 27 Area X neurons for a low CV value (left plot) and a high CV value (right box). Figure convention same as in (E). Data correspond to green arrows in (C). Vertical bar is 500 uV.

Bird	LMAN CV median ± SEM	Area X CV median ± SEM	Wilcoxon ranksum test
ZF-1	0.77 ± 0.02	0.28 ± 0.0024	$p < 1E^{-160}$ | 1.54E-161
ZF-2	1.69 ± 0.04	0.61 ± 0.01	$p < 1E^{-71}$ | 3.23E-72
ZF-3	0.75 ± 0.02	0.27 ± 0.00	$p < 1E^{-314}$ | 3.13E-315
ZF-4	1.44 ± 0.06	0.67 ± 0.01	$p < 1E^{-55}$ | 6.01E-56
ZF-5	1.64 ± 0.04	1.04 ± 0.01	$p < 1E^{-81}$ | 1.03E-82
Population median	**1.44 ± 0.21**	**0.61 ± 0.14**	

Table 2: Median CV values were significantly higher for LMAN neurons compared to Area X neurons. Median values ± SEM. Population statistics are computed across median CVs. p value is the result of a Wilcoxon rank sum test.

Bird	LMAN: CV versus δ/γ			Area X: CV versus δ/γ	
	R	p		R	p
ZF-1	0.64	5.84E-59		0.68	2.46E-68
ZF-2	0.50	1.92E-22		0.06	0.2479
ZF-3	0.36	5.52E-32		0.25	4.19E-15
ZF-4	0.17	0.0025		-0.28	4.56E-07
ZF-5	0.69	1.21E-55		-0.01	0.8525

Table 3: LMAN CV values were significantly and positively correlated with δ/γ values for 5/5 zebra finches. Correlations for Area X neurons were more heterogeneous. R, Pearson correlation coefficient.

Synchronized population bursting in LMAN during sleep is associated with a negative deflection in the LFP

Our findings suggested that within LMAN, populations of neurons are co-activated during specific time points in sleep. In order to explore the synchronized bursting of LMAN neurons during sleep - and how they are related to the LFP (**Fig. 6A**) - we identified and thresholded bursting events in the population of LMAN neurons (**Fig. 6B**). Then, we used these synchronized bursts to identify activity patterns in the LFP, which we called “burst-aligned LFP” (**Fig. 6C**). Individual burst-aligned LFP segments generally had higher power in frequency ranges < 10 Hz (example in **Fig. 6D**), and the average burst-aligned LFP showed a prominent low-frequency power burst centered on zero-time lag (**Fig. 6E**). Indeed, when we compared the bursting-aligned LFP segments (**Fig. 6F, blue line**) to randomly shifted LFP segments (**Fig. 6F, black line)**, the bursting-aligned LFP segments showed a notable increase in power for frequencies lower than 10 Hz. This phenomenon was present across birds (**Fig. 6G).** Every bird examined had a notable negative deflection that corresponded to the

population synchronized bursting (**Fig. 6H**). Importantly, this negative deflection did not always occur at exactly zero-time lag; in most cases it preceded the population burst.

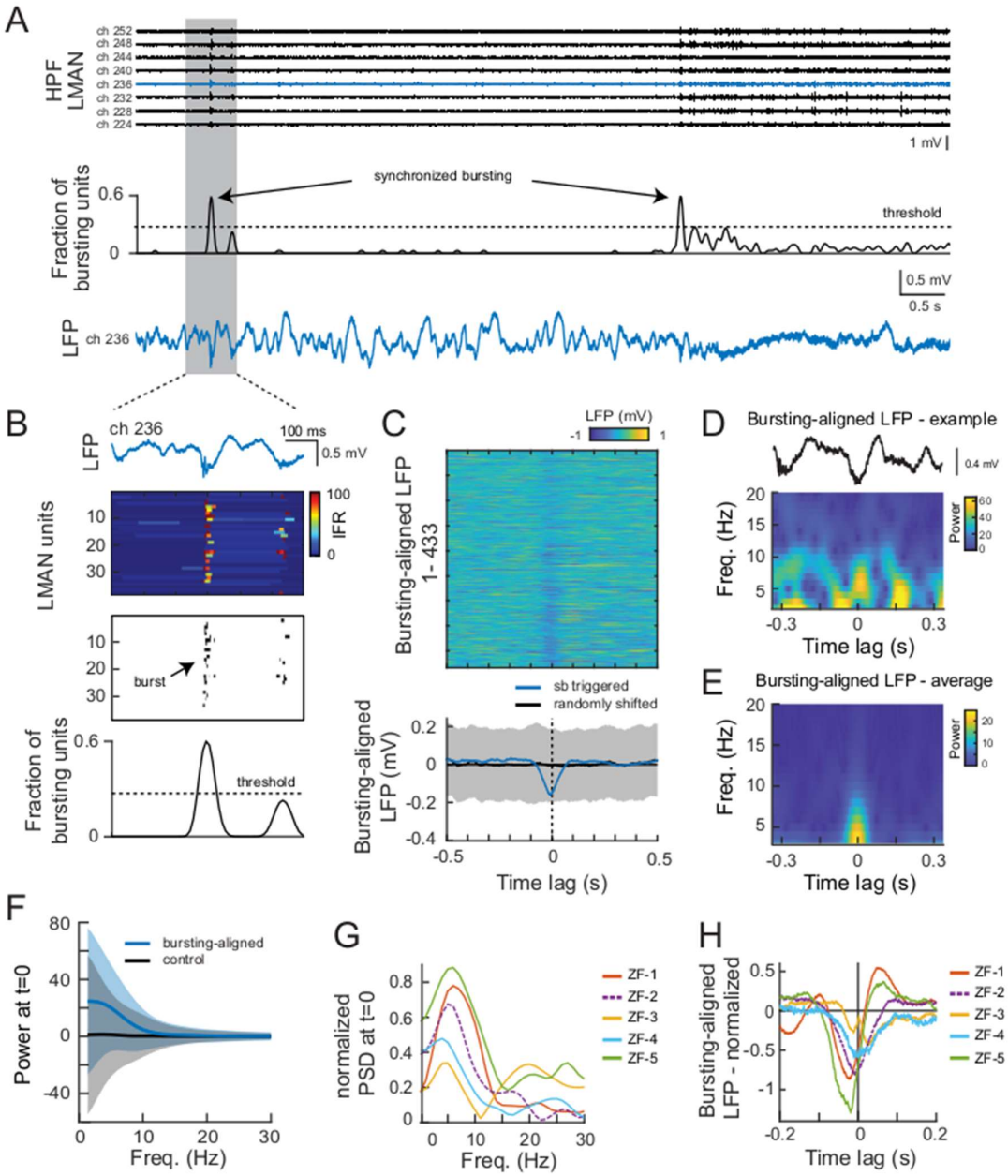

Figure 6: Synchronized bursting in LMAN is associated with a negative deflection in the LFP (A) Two examples of synchronized bursting activity in LMAN from ZF-2 (r15v15). Top panel depicts high-pass filtered (HPF) electrode signals from eight electrodes in LMAN. Middle panel depicts the detection of synchronized bursting (black line) based on the fraction of bursting units in a 50 ms window exceeding the 97.5th percentile threshold. Bottom panel depicts the raw LFP (blue, same electrode as in top panel). Area indicated by gray shading is expanded in (B). **(B)** Zoom-in on the highlighted gray window in (A). Top panel depicts the instantaneous firing rate (IFR) of all LMAN units (n = 32), color-coded and clipped at 100 Hz. The panel below depicts the occurrence of bursts in black for each LMAN unit. Lower panels same as in (A). **(C)** Upper panel depicts 433 bursting-aligned LFP segments detected from ch 236, stacked and color-coded. Events are sorted by the total fraction of bursting units. Lower panel indicates the average bursting-aligned LFP (blue) and the same statistics for randomly shifted LFP segments (black, gray shows +/- SD). **(D)** A raw data example of a bursting-aligned LFP (top panel) and its spectrogram (bottom panel; 320 ms window, 20 ms shift size). **(E)** The average bursting aligned-LFP spectrogram. **(F)** Average power density at time of a synchronized burst detection (blue line) compared to data from randomly shifted control LFP segments (black line). Note how the power density for the synchronized burst is elevated at low frequencies. **(G)** Bursting-aligned LFP deflections have a prominent increase in power around 5 Hz. Shown is the power spectral density (PSD) at t=0 subtracted by the average PSD of the randomly shifted control, and divided by the SD for each bird. **(H)** LFP show consistent negative dip during a synchronized burst. Each line indicates the bursting-aligned LFP normalized to a randomly shifted control (z-norm) for each bird. Note that the trough occurs before 0-time lag in most birds.

Synchronized population bursts in LMAN occur predominantly during NREM sleep

We were curious as to whether these synchronized bursting events in LMAN occurred during a specific sleep regime, i.e. either during NREM sleep (i.e., SWS and IS sleep) or during REM sleep (**Fig. 7A**). With the exception of 1 bird (**Fig 7A, ZF-4: upward triangle**), the synchronized bursting events occurred predominantly during NREM sleep.

We also examined the δ/γ values surrounding the synchronized bursting events, with the expectation that these events might occur during LFP segments with higher δ/γ values (i.e., during SWS). Interestingly, we found that the bursting events were associated with lower δ/γ values compared to control events for all 5 birds (**Fig. 7B**; **Fig. 7 Supplement 2**; see Methods for details). Because the δ/γ is a ratio, low δ/γ values can result from a decrease in δ power or an increase in γ power. We examined the δ and γ power separately for bursting events compared to control events. We found that while the power in the δ range was indeed elevated during bursting events compared to control events (**Fig. 7C**), a larger increase in γ power during the bursting event (**Fig. 7D)** compared to control segments led to the overall lower δ/γ values we observed during bursting events compared to controls (**Fig. 7B**).

When visualized as the difference between the burst and control segments (**Fig. 7E**), this burst-associated increase in power extended from delta up through high gamma and was present for all birds analyzed (**Fig. 7F**).

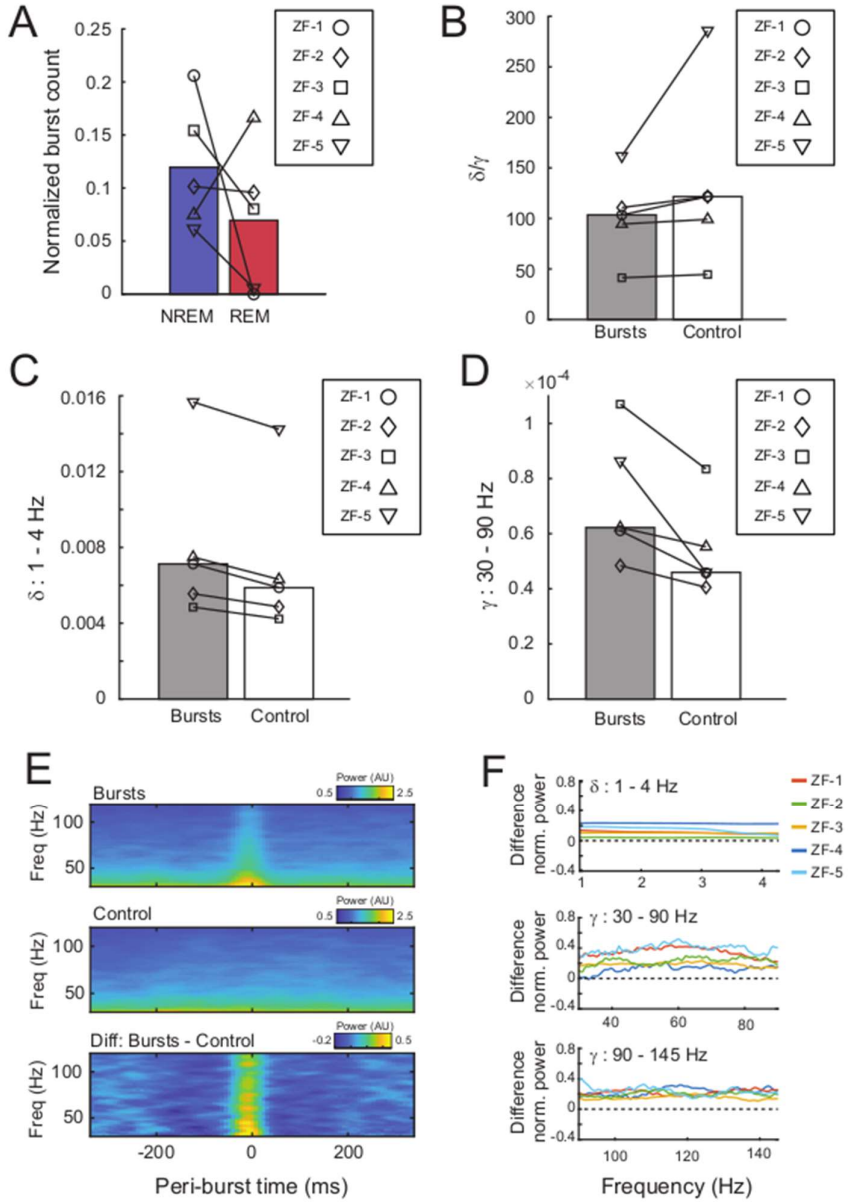

Figure 7: Synchronized bursts occur during NREM sleep and are associated with higher γ activity. (A) Bar plots indicate mean number of bursts associated with each sleep state normalized by the overall sleep state duration in seconds (see Figure 7 Supplement 1). With the exception of ZF-4, most birds showed more bursts detected during NREM states compared to REM sleep states. NREM states included both SWS and IS classified states. Symbols indicate median data for each bird. **(B)** Bar plots indicate mean δ/γ value calculated for 500 ms segments of LFP that were centered on a synchronized burst detection (Bursts, yellow bar) compared to the mean value of 500 ms control segments of LFP that were temporally shifted away from the burst detection by a random offset (Control, gray bar; see Methods for details). Symbols indicate median data for each bird. Note how δ/γ values are on average higher for the control LFP segments. **(C)** Same convention as in (B) for δ values. Note how δ values are higher for the burst LFP segments compared to the control LFP segments. See also Figure 7 Supplement 2. **(D)** Same convention as in (B) and (C) for γ values. Note the higher γ values during the burst LFP segments compared to the control LFP segments. **(E)** Spectrograms display the average peri-burst time window surrounding a burst event (top), a control event (middle), and the difference in power between the burst event and the control event (bottom) for ZF-2. Note the increase in power surrounding the burst event that extends up into the high γ range. **(F)** Panels display the normalized PSD for different frequency ranges: δ (1-4 Hz, top), low γ (30-90 Hz, middle), and high γ (90-145 Hz, bottom plot). Normalized PSD indicates the difference between the burst events and the control events divided by the standard deviation of the control events. Different line colors indicate different

birds. Note how data for all birds fall above the zero (dotted line) indicating higher values during the burst event compared to control events.

Discussion

In order to explore the activity patterns of the AFP during sleep in songbirds and specifically how they may relate functionally to mammalian cortico-striatal circuit activity, we investigated the sleep-related activity patterns of neurons in LMAN and Area X (Fig. 1A, C) using chronically implanted Neuropixels probes (Fig. 1B).

Coherence between field potentials has been used in a multitude of studies as a mesoscopic measure of functional connectivity between brain areas (Schneider et al., 2021) and is believed to reflect the neuronal connectivity (Buzsáki & Schomburg, 2015) and oscillatory synchronization (Bastos et al., 2015) in these brain areas. Contrary to our expectations, we did not observe strong cross-area coherence between LMAN and Area X on average, although individual LMAN-Area X pairs did show strong coherence > 0.5. By contrast, studies of motor skill learning in rodents found an increase in cross-area coherence between motor cortex and striatum during sleep (Koralek et al., 2013; Lemke et al., 2021). The fact that we did not observe strong cross-area coherence may stem from the fundamental differences in motor learning paradigms or that birds in this study were not actively engaged in a learning paradigm.

During sleep, we observed that populations of LMAN neurons spontaneously reactivated in bursting events. These events occurred predominantly during NREM sleep and were associated with an increase in gamma band power. Across animals, the population bursting events were preceded by a large negative deflection of the LFP, pointing to the possibility that they were triggered by the ongoing large-scale global oscillatory activity in LMAN.

The combination of large negative LFP deflection and population bursting activity in LMAN is highly reminiscent of SWR activity observed during SWS in rodent hippocampus (Buzsáki, 1986, 2015; O'Keefe, 1976).

Importantly, the sharp wave and ripple LFP patterns that characterize SWRs are thought to arise from the specific anatomy of the hippocampus. The sharp wave reflects massive excitation of CA1 neurons by the pyramidal cells in CA3. This excitation synchronizes the interneuron network and generates a ripple in the pyramidal layer (Buzsáki et al., 1983; Girardeau & Zugaro, 2011; Liu et al., 2022). In rodents, the ripple oscillation is characterized by a frequency in the range of 110-200 Hz, overlapping with typical gamma band activity (Buzsáki, 2015; Liu et al., 2022).

Our observation of SWR-like activity in LMAN suggests that sharp wave and ripple LFP patterns may not be unique to mammalian hippocampus. Indeed, similar LFP patterns have been recorded during sleep in the reptilian pallial area known as the dorsal ventricular ridge (Albeck et al., 2022; Libourel et al., 2018; Shein-Idelson et al., 2016), suggesting that multiple neural architectures may give rise to these activity patterns. However, the function of this non-hippocampal SWR-like activity remains unclear.

Hippocampal SWR activity has been typically considered as a biomarker that accompanies spatial navigation learning and episodic memory (Buzsáki, 2015); these learning paradigms

are fundamentally different from the auditory and motor learning that characterizes vocal learning in songbirds. Furthermore, the birds used in our and the cited studies sang mature crystallized songs characterized by stable motif structure, suggesting that the developmental learning period had already ended. Nevertheless, LMAN has been shown to have an important role in the ongoing maintenance of adult song (Brainard & Doupe, 2000; Solis et al., 2000; Warren et al., 2011) via N-methyl-D-aspartate (NMDA) receptor-dependent transmission from LMAN to the pallial premotor nucleus RA (Brainard & Doupe, 2000; Solis et al., 2000; Warren et al., 2011). Bursting in LMAN influences RA and thereby affects the spectral variability of song (Kao et al., 2005; Moorman et al., 2021; Tian et al., 2023; Woolley & Kao, 2015). From these observations a potential role of SWR activity emerges in the consolidation of experience in a broader sense (Tachibana et al., 2022).

"Replay"-like reactivations have also been reported during sleep in the RA (Dave & Margoliash, 2000; Elmaleh et al., 2021, 2023). Given the widespread LFP dynamics that we observed across LMAN, it would be important to investigate how bursting in LMAN and RA are temporally related, and specifically whether the widespread LFP oscillations in LMAN influence RA bursting during sleep.

Materials and Methods

Subjects

Seven male zebra finches (*Taeniopygia guttata*) were used in this study; data were pooled across two laboratories in France (the Neuroscience Paris-Saclay Institute and the Bordeaux Neurocampus). The age of the animals ranged from 66 days post-hatch (dph) to 232 dph at the time of recording. The animals were bred and housed in the animal facilities of the laboratories. During the experiment, animals were housed individually with water and food *ad libitum* under a 14:10 hr light/dark cycle. The description of the dataset can be found in the repository where the data is stored. https://gin.g-node.org/E4-Leblois/npx_sleep_2024/src/master/dataset/participants.xlsx
All experimental procedures were approved by the French Ministry of Research and the ethical committee ``Paris-Sud et Centre'' (CEEA No. 59, project 2017-25) and "Poissons Oiseaux Nouvelle Aquitaine" (CEEA No. 73, project S73) and performed under the license 2015-25 and APAFIS#13413-2018020713145795.

Surgery and experiments

Surgery

The day of the surgery, food and water sources were removed from the cage approximately 30 minutes before the start of the surgery. Animals were anesthetized with isoflurane (0.6-1.5\% inhalation) and placed in the stereotactic apparatus once the flexion reflex was no longer observable. 0.05 microliters of diluted lidocaine (0.5mg/kg) was administered subcutaneously and a local anesthetic (0.5 g Emla® creme) was applied to the exposed head skin along the caudo-rostral axis after removing feathers and disinfecting the area with ethanol and betadine. The scalp was resected and the exposed skull was prepared for the implant by drilling several small holes in the outer bone layer. A small craniotomy contralateral to the final implant was made to place a silver wire in contact with the dura that served as the electrical ground.

556
557 The main craniotomy was made on the right hemisphere around 1.7 mm lateral to the superior
558 sagittal sinus and 4.5 mm anterior to lambda, the confluence of sinuses, with the flat part of
559 the anterior skull rotated to a 50-degree angle. The positions of LMAN and Area X were
560 mapped with high-impedance single-electrodes in order to identify the brain areas based on
561 the firing rate properties thereof.
562
563 A Neuropixels probe version 1.0 (Jun et al., 2017) was implanted 4 to 5 mm deep to penetrate
564 the estimated center of LMAN and Area X. The custom-made holder that carried the
565 Neuropixels probe was fixed to the skull with dental cement and the craniotomy was sealed
566 with a two-part silicone gel (Dow Dowsil™) before it was covered with a custom-made casing.
567 In contrast to the Neuropixels probe, the headstage was fixed with the bird's head in the
568 stereotactic system rotated to 35 degrees, which corresponded to the natural position of the
569 birds' head. Finally, the ground wire was connected and open holes along the implant were
570 sealed with fast drying two-component silicone gel (Kwik-Sil). Immediately after the surgery,
571 a weight reliever with adjustable counterweight was added to help the animals cope with the
572 additional weight of the implant (~1.9 g).

573 **Histology and electrode channel mapping**

574 Post-hoc control of the electrode location in the brain was performed through histological
575 examination of brain tissue. Birds were sacrificed at the end of the experiment with a lethal
576 intraperitoneal injection of Exagon (pentobarbital sodium, 400 mg/mL), and in some cases
577 perfused intracardially (PBS 0.01 M sometimes followed by 4% paraformaldehyde (PFA) as
578 fixative). The brain was removed and post-fixed in 4% PFA for at least 24 hr. We then cut the
579 right hemisphere along the sagittal plane either with a freezing microtome whenever the brain
580 was additionally cryoprotected in 30% sucrose (n=4 cases), or with a vibratome in slices of 50
581 or 80-micron thickness, respectively. Images of the individual brain slices were taken by
582 means of bright-field and epiflurescence microscopy and analyzed using ImageJ software
583 (Rasband WS, NIH, Bethesda, Maryland, USA). The electrode track as indicated by
584 colored/fluorescent dye, was clearly visible on consecutive brain slices (see Fig. 1C).
585
586 We defined the boundaries of LMAN and Area X based on darkness of the tissue in regular
587 light or the fluorescent background, as these two brain areas showed a clear contrast with
588 surrounding tissue due to higher myelination, cell density, and size (Niwdorf-Begweiler and
589 Bishof, 2007). The reconstruction of electrode channels to be assigned to LMAN or X was
590 performed based on the location of the electrode tip on the histological pictures, the
591 coordinates of the channels on the electrode and the above-mentioned boundaries of LMAN
592 and X. The limits of LMAN were also confirmed based on spontaneous activity, including more
593 bursts of large spikes in LMAN as compared to surrounding tissue.

594 **Data acquisition**

595 Animals were housed individually in sound-attenuated recording chambers and neural
596 recordings were performed in sessions (one to 24 hours of continuous neural recording).
597 Sleep-related activity was recorded either continuously throughout the night or at specific
598 times at the beginning or end of the night. In the case of whole-night recordings, a one-hour
599 snippet was selected for further analysis (see Table 4). Extracellular activity was recorded with
600 the chronically implanted Neuropixels 1.0 probe which splits the signal on chip and samples

the spike signal (bandpass filtered at 0.3 and 10 kHz) at 30 kHz and the LFP signal (bandpass filtered at 0.5 and 500 Hz) at 2500 Hz. Audio signals were simultaneously recorded using a wall-attached microphone, pre-amplified and digitized at 10, 20 or 32 kHz depending on the bird (more information available in our repository's metadata). Additionally, videos were recorded and used to confirm sleeping behavior in four birds (0.5 or 0.2 fps). Extensive information on the dataset can be found in the repository where our data is stored.

ZF	Animal ID	Start of recording	Data available	Age at recording (dph)	# LMAN units	# Area X units	Video recording
1	g4r4	03:58 pm *	LFP+SU**	84	30	26	no
2	r15v15	8:42 pm	LFP+SU	125	32	6	no
3	j8v8	05:18 am	LFP+SU	124	40	19	no
4	Redred	05:30 am	LFP+SU	177	28	7	yes
5	r5n5	5:21 pm *	LFP+SU	85	6	3	yes
6	black/cyan	04:17 am	LFP	232	na	na	no
7	no_label	00:28 am	LFP	76	na	na	yes

* night time initiated earlier than normal
** SU: spike sorted single and multi-unit activity from high-pass filtered voltage traces
Table 4: Information related to experimental animals

Data analysis

Data preprocessing and spike clustering

For neural spiking analysis, spike sorting was performed in four of the seven birds on all active channels using Kilosort 2.0 and Kilosort 2.5 (Pachitariu et al., 2016) and manually curated using phy (https://github.com/kwikteam/phy) in four birds (ZF-1 to -3 and ZF-5) or automatically curated using SpikeInterface (script available in our data repository) in one bird (ZF-4).

Sleep staging

The sleep staging was performed based on a previously described automated method in songbirds that classifies sleep periods in an unsupervised manner depending on multiple features of EEG signals (Canavan & Margoliash, 2020; Low et al., 2008). Since we did not have EEG measurements, we computed the sleep stages from an LMAN LFP channel (identified medially located LMAN channel along the dorsoventral axis of recording) with bins of 3 s and a window shift of 1 sec. Spectral parameters were computed from the multi-taper spectral analysis (Prerau et al. 2016) of the down sampled (250 Hz) LFP. Even though this

process resulted in classification into 3 sleep stages, REM, SWS, and IS, the number of bins classified as IS was much smaller and shorter in duration (Figure 7). So, for the coherence analysis, we continued with only the bins identified as either REM or SWS.
We also excluded any bins that overlapped with movement artifacts in the microphone signal. To identify movements in the microphone data, each 1-second bin was labeled as 'potential movement' when a sustained artifact larger than *n* times the signal's chunk mean noise minus the standard deviation of the same chunk was observed (where *n* is determined by visual inspection of the microphone's amplitude envelope and spectrogram).

LFP Coherence Analysis

The computation of coherence was done as follows (see Figure 4 Supplement 1): first, we extracted the LFP data from *.bin* files utilizing SpikeInterface (https://spikeinterface.readthedocs.io/en/latest/overview.html) with phase shift correction using *spikeinterface.preprocessing.phase_shift*. Next, we removed artifacts from the LFP signal by establishing a threshold based on 80% of the maximum absolute trace value and interpolating the signal around the artifact time point with a margin of 20 sample points before and after. Next, we z-scored the trace using *elephant.signal_processing.zscore*. After that, we identified consecutive, artifact-free six seconds within the same state (*chunk_length*). We used six seconds to guarantee at least six cycles for our lowest frequency of interest (FOI), *i.e.,* 1Hz. Afterwards, we determined the number of available chunks for each sleep state, and what was the common minimum between states (*n_chunks*), since SWS's available chunks were often more numerous than REM's (Figure 7 Supplement 1). In order to ensure enough computation resolution for the coherency population analysis, we included only birds that had at least 15 *n_chunks.* For the n = 7 birds that were included in the analysis, the total percentage of data that were analyzed ranged from 12% to 55%. We then proceeded to segment and concatenate LFP data with the same *n_chunks* for REM and SWS sleep states. Finally, we computed the coherence between every 4th LFP channel spanning Area X and LMAN. Specifically, we compute the magnitude squared coherence, CL1L2, of LFP signals L1 and L2 as follows:

$$CL1L2 = |(PL1L2)|^2/(PL1L1*PL1L1)$$

where PL1L1 and PL1L1 are power spectral density estimates of L1 and L2 using Welch's method, and |PL1L2| is the absolute value of the cross spectral density estimate. We used the *scipy.signal.coherence (https://docs.scipy.org/doc/)* with the number of points per segment (*nperseg)* equal to *chunk_length* (6 seconds) multiplied by the signal's sampling frequency (i.e., 6 seconds in sample points), with no overlap, and detrending set to '*constant'*. The Python scripts used for this analysis can be found in our data repository.

Analysis of spiking variability

Temporal variability in spiking activity was assessed using the coefficient of variation (CV) in consecutive, non-overlapping segments of 10 seconds. Within each segment, the total number of spikes (ns, from all units either in LMAN or in Area X) was counted in sub-windows of 20 milliseconds. The CV was then computed as the standard deviation of spike counts divided by the mean spike count across all sub-windows within that segment (CV $=\sigma_{ns}/\mu_{ns}$). δ/γ ratios were computed for the LFP signal of the central electrode in LMAN in the same 10-second segment. Pearson's correlation coefficient (Pearson, 1895) and type-II linear

regression (Ricker, 1973) were used to assess the relationship between Delta/Gamma ratio and the CV of spike activation. The average firing rate of neurons in LMAN and Area X was calculated by determining the total spike count per second within the same windows where CV was computed.

Population synchronized burst detection and spectral analysis of associated LFP

For each neural unit (single or multiunit), bursts were identified when the Instantaneous Firing Rate (IFR) exceeded 100 Hz. The fraction of simultaneously bursting LMAN units was determined in a sliding 50 ms window with 10 ms step size. The resulting trace was smoothed using a Gaussian kernel with 15 ms standard deviation, and candidate events of synchronized bursts were classified as peaks exceeding the 97.5th percentile.

To create control events, we temporally shifted the time points of synchronized bursts by a random offset between -1 and 1 second, sampled from a uniform distribution. For assessing the LFP around synchronized bursts and control time points, we selected the central LMAN LFP and compared raw traces.

For detailed temporal resolution of the power density, we plotted the spectral decomposition using 320 ms-long windows with a 20 ms step size. This was achieved with Matlab's `spectrogram` function, which employs a short-time Fourier transform, as illustrated in Figures 6D and 6E.

The power spectral density (PSD) shown in Figures 6F and 6G was estimated for the central LMAN LFP trace within the 320 ms surrounding the event time points using Welch's method (`pwelch` function in Matlab). In Figure 6G, to normalize the PSD at synchronized bursts, we subtracted the average control PSD and divided the result by the standard deviation of the control PSD. This normalization was performed to account for differences in magnitude across birds.

All spectral analyses in Figure 7 were conducted on 500 ms windows centered around the event time.

Data availability

All research data as well as scripts to replicate the results are available in the corresponding repository: https://gin.g-node.org/E4-Leblois/npx_sleep_2024

Spectral analysis and visualizations in Figure 3 were computed with an adapted code of the following repository https://github.com/cortex-lab/spikes.

Funding

AD: This research was supported by the 'Agence Nationale de la Recherche' (project SleepinBrainDyn) and from the CNRS (International Emerging Action, project BirdSleep).

EGZC received the EUR/7410-5 EUR NEURO and GP/7200R-12 GPR BRAIN_2030 funding for her PhD contract.

JMO: This research was funded by grants from the German Research Foundation (Deutsche Forschungsgemeinschaft; ON 151/1-1) and the Daimler and Benz Foundation (PN 32-09/18).

CL, HY, NG, and JMO were also supported by the BayFrance program (FK23 2019).

Competing interest

The authors declare that the research was conducted in the absence of any commercial or financial relationships that could be construed as a potential conflict of interest.

Author Contributions

Author	CL	AD	EGZC	HY	RD	RU	AR	NG	AL	RHRH	JMO
Conceptualization	x							X	X		X
Methodology	x	X	X	X		X	X	X	X	X	X
Software	x	X	X	X							
Validation	x	X						X	X		X
Formal Analysis	x	X	X	X	X				X		X
Investigation	x	X	X	X							
Writing – Original Draft	x	X	X								X
Writing – Review & Editing	x	X	X					X	X	X	X
Resources								X	X		X
Data Curation	x	X	X								
Visualization	x	X	X	X							X
Supervision								X	X	X	X
Project Administration								X	X		X
Funding Acquisition								X	X		X

Acknowledgements

JMO would like to thank Harald Luksch for support of this research. We would further like to thank and acknowledge Melanie Dumont for excellent animal caretaking and Manon Rolland for help with experiments.

References

Albeck, N., Udi, D. I., Eyal, R., Shvartsman, A., & Shein-Idelson, M. (2022). Temperature-robust rapid eye movement and slow wave sleep in the lizard Laudakia vulgaris. *Communications Biology*, *5*(1), Article 1. https://doi.org/10.1038/s42003-022-04261-4

Ali, F., Otchy, T. M., Pehlevan, C., Fantana, A. L., Burak, Y., & Ölveczky, B. P. (2013). The Basal Ganglia Is Necessary for Learning Spectral, but Not Temporal, Features of Birdsong. *Neuron*, *80*(2), 494–506. https://doi.org/10.1016/j.neuron.2013.07.049

Andalman, A. S., & Fee, M. S. (2009). A basal ganglia-forebrain circuit in the songbird biases motor output to avoid vocal errors. *Proceedings of the National Academy of Sciences of the United States of America*, *106*(30), 12518–12523. https://doi.org/10.1073/pnas.0903214106

Bastos, A. M., Vezoli, J., & Fries, P. (2015). Communication through coherence with inter-areal delays. *Current Opinion in Neurobiology*, *31*, 173–180. https://doi.org/10.1016/j.conb.2014.11.001

Bottjer, S. W., Miesner, E. A., & Arnold, A. P. (1984). Forebrain lesions disrupt development but not maintenance of song in passerine birds. *Science (New York, N.Y.)*, *224*(4651), 901–903. https://doi.org/10.1126/science.6719123

Brainard, M. S., & Doupe, A. J. (2000). Interruption of a basal ganglia-forebrain circuit prevents plasticity of learned vocalizations. *Nature*, *404*(6779), 762–766. https://doi.org/10.1038/35008083

Buzsáki, G. (1986). Hippocampal sharp waves: Their origin and significance. *Brain Research*, *398*(2), 242–252. https://doi.org/10.1016/0006-8993(86)91483-6

Buzsáki, G. (2015). Hippocampal sharp wave□ripple: A cognitive biomarker for episodic memory and planning. *Hippocampus*, *25*(10), 1073–1188. https://doi.org/10.1002/hipo.22488

Buzsáki, G., & Draguhn, A. (2004). Neuronal Oscillations in Cortical Networks. *Science*, *304*(5679), 1926–1929. https://doi.org/10.1126/science.1099745

Buzsáki, G., Leung, L. W. S., & Vanderwolf, C. H. (1983). Cellular bases of hippocampal EEG in the behaving rat. *Brain Research*, *287*(2), 139–171.

Buzsáki, G., & Schomburg, E. W. (2015). What does gamma coherence tell us about inter-regional neural communication? *Nature Neuroscience*, *18*(4), 484–489. https://doi.org/10.1038/nn.3952

Buzsáki, G., & Wang, X.-J. (2012). Mechanisms of Gamma Oscillations. *Annual Review of Neuroscience*, *35*, 203–225. https://doi.org/10.1146/annurev-neuro-062111-150444

Canavan, S. V., & Margoliash, D. (2020). Budgerigars have complex sleep structure similar to that of mammals. *PLOS Biology*, *18*(11), e3000929. https://doi.org/10.1371/journal.pbio.3000929

Cardin, J. A. (2016). Snapshots of the Brain in Action: Local Circuit Operations through the Lens of γ Oscillations. *Journal of Neuroscience*, *36*(41), 10496–10504. https://doi.org/10.1523/JNEUROSCI.1021-16.2016

Cardin, J. A., Carlén, M., Meletis, K., Knoblich, U., Zhang, F., Deisseroth, K., Tsai, L.-H., & Moore, C. I. (2009). Driving fast-spiking cells induces gamma rhythm and controls sensory responses. *Nature*, *459*(7247), 663–667. https://doi.org/10.1038/nature08002

Csicsvari, J., Hirase, H., Czurko, A., & Buzsáki, G. (1998). Reliability and state dependence of pyramidal cell-interneuron synapses in the hippocampus: An ensemble approach in the behaving rat. *Neuron*, *21*(1), 179–189. https://doi.org/10.1016/s0896-6273(00)80525-5

Dave, A. S., & Margoliash, D. (2000). Song replay during sleep and computational rules for sensorimotor vocal learning. *Science (New York, N.Y.)*, *290*(5492), 812–816. https://doi.org/10.1126/science.290.5492.812

Debas, K., Carrier, J., Barakat, M., Marrelec, G., Bellec, P., Hadj Tahar, A., Karni, A., Ungerleider, L. G., Benali, H., & Doyon, J. (2014). Off-line consolidation of motor

sequence learning results in greater integration within a cortico-striatal functional network. *NeuroImage*, *99*, 50–58. https://doi.org/10.1016/j.neuroimage.2014.05.022

Derégnaucourt, S., Mitra, P. P., Fehér, O., Pytte, C., & Tchernichovski, O. (2005). How sleep affects the developmental learning of bird song. *Nature*, *433*(7027), 710–716. https://doi.org/10.1038/nature03275

Duffy, A., Latimer, K. W., Goldberg, J. H., Fairhall, A. L., & Gadagkar, V. (2022). Dopamine neurons evaluate natural fluctuations in performance quality. *Cell Reports*, *38*(13), 110574. https://doi.org/10.1016/j.celrep.2022.110574

Elmaleh, M., Kranz, D., Asensio, A. C., Moll, F. W., & Long, M. A. (2021). Sleep replay reveals premotor circuit structure for a skilled behavior. *Neuron*, *109*(23), 3851-3861.e4. https://doi.org/10.1016/j.neuron.2021.09.021

Elmaleh, M., Yang, Z., Ackert-Smith, L. A., & Long, M. A. (2023). Uncoordinated sleep replay across hemispheres in the zebra finch. *Current Biology*, *33*(21), 4704-4712.e3. https://doi.org/10.1016/j.cub.2023.09.005

Farries, M. A., Ding, L., & Perkel, D. J. (2005). Evidence for “direct” and “indirect” pathways through the song system basal ganglia. *The Journal of Comparative Neurology*, *484*(1), 93–104. https://doi.org/10.1002/cne.20464

Farries, M. A., & Perkel, D. J. (2002). A Telencephalic Nucleus Essential for Song Learning Contains Neurons with Physiological Characteristics of Both Striatum and Globus Pallidus. *Journal of Neuroscience*, *22*(9), 3776–3787. https://doi.org/10.1523/jneurosci.22-09-03776.2002

Girardeau, G., & Zugaro, M. (2011). Hippocampal ripples and memory consolidation. *Current Opinion in Neurobiology*, *21*(3), 452–459. https://doi.org/10.1016/j.conb.2011.02.005

Graybiel, A. M. (2008). Habits, rituals, and the evaluative brain. *Annual Review of Neuroscience*, *31*, 359–387. https://doi.org/10.1146/annurev.neuro.29.051605.112851

Grunow, A., & Neuringer, A. (2002). Learning to vary and varying to learn. *Psychonomic Bulletin & Review*, *9*(2), 250–258. https://doi.org/10.3758/BF03196279

Gulati, T., Ramanathan, D. S., Wong, C. C., & Ganguly, K. (2014). Reactivation of emergent task-related ensembles during slow-wave sleep after neuroprosthetic learning. *Nature Neuroscience*, *17*(8), Article 8. https://doi.org/10.1038/nn.3759

Hahnloser, R. H. R., & Fee, M. S. (2007). Sleep-related spike bursts in HVC are driven by the nucleus interface of the nidopallium. *Journal of Neurophysiology*, *97*(1), 423–435. https://doi.org/10.1152/jn.00547.2006

Hahnloser, R. H. R., Kozhevnikov, A. A., & Fee, M. S. (2006). Sleep-Related Neural Activity in a Premotor and a Basal-Ganglia Pathway of the Songbird. *Journal of Neurophysiology*, *96*(2), 794–812. https://doi.org/10.1152/jn.01064.2005

Jun, J. J., Steinmetz, N. A., Siegle, J. H., Denman, D. J., Bauza, M., Barbarits, B., Lee, A. K., Anastassiou, C. A., Andrei, A., Aydın, Ç., Barbic, M., Blanche, T. J., Bonin, V., Couto, J., Dutta, B., Gratiy, S. L., Gutnisky, D. A., Häusser, M., Karsh, B., … Harris, T. D. (2017). Fully integrated silicon probes for high-density recording of neural activity. *Nature*, *551*(7679), 232–236. https://doi.org/10.1038/nature24636

Kao, M. H., Doupe, A. J., & Brainard, M. S. (2005). Contributions of an avian basal ganglia–forebrain circuit to real-time modulation of song. *Nature*, *433*(7026), 638–643. https://doi.org/10.1038/nature03127

Kawai, R., Markman, T., Poddar, R., Ko, R., Fantana, A. L., Dhawale, A. K., Kampff, A. R., & Ölveczky, B. P. (2015). Motor Cortex Is Required for Learning but Not for Executing a Motor Skill. *Neuron*, *86*(3), 800–812. https://doi.org/10.1016/j.neuron.2015.03.024

Knowlton, B. J., Mangels, J. A., & Squire, L. R. (1996). A neostriatal habit learning system in humans. *Science (New York, N.Y.)*, *273*(5280), 1399–1402. https://doi.org/10.1126/science.273.5280.1399

Kobak, D., Pardo-Vazquez, J. L., Valente, M., Machens, C. K., & Renart, A. (2019). State-dependent geometry of population activity in rat auditory cortex. *eLife*, *8*. https://doi.org/10.7554/eLife.44526

Konishi, M. (1965). The role of auditory feedback in the control of vocalization in the white-crowned sparrow. *Zeitschrift Für Tierpsychologie*, *22*(7), 770–783.

Konishi, M. (1970). Comparative neurophysiological studies of hearing and vocalizations in songbirds. *Zeitschrift Für Vergleichende Physiologie*, *66*(3), 257–272. https://doi.org/10.1007/BF00297829

Koralek, A. C., Costa, R. M., & Carmena, J. M. (2013). Temporally Precise Cell-Specific Coherence Develops in Corticostriatal Networks during Learning. *Neuron*, *79*(5), 865–872. https://doi.org/10.1016/j.neuron.2013.06.047

Lemke, S. M., Ramanathan, D. S., Darevksy, D., Egert, D., Berke, J. D., & Ganguly, K. (2021). Coupling between motor cortex and striatum increases during sleep over long-term skill learning. *eLife*, *10*, 1–25. https://doi.org/10.7554/eLife.64303

Libourel, P. A., Barrillot, B., Arthaud, S., Massot, B., Morel, A. L., Beuf, O., Herrel, A., & Luppi, P. H. (2018). Partial homologies between sleep states in lizards, mammals, and birds suggest a complex evolution of sleep states in amniotes. *PLoS Biology*, *16*(10), e2005982. https://doi.org/10.1371/journal.pbio.2005982

Liu, A. A., Henin, S., Abbaspoor, S., Bragin, A., Buffalo, E. A., Farrell, J. S., Foster, D. J., Frank, L. M., Gedankien, T., Gotman, J., Guidera, J. A., Hoffman, K. L., Jacobs, J., Kahana, M. J., Li, L., Liao, Z., Lin, J. J., Losonczy, A., Malach, R., … Buzsáki, G. (2022). A consensus statement on detection of hippocampal sharp wave ripples and differentiation from other fast oscillations. *Nature Communications*, *13*(1), Article 1. https://doi.org/10.1038/s41467-022-33536-x

Low, P., Shank, S. S., Sejnowski, T. J., & Margoliash, D. (2008). Mammalian-like features of sleep structure in zebra finches. *Proc Natl Acad Sci U S A*, *105*(26), 9081–9086. https://doi.org/0703452105 [pii]10.1073/pnas.0703452105

Margoliash, D., & Schmidt, M. F. (2010). Sleep, off-line processing, and vocal learning. *Brain and Language*, *115*(1), 45–58. https://doi.org/10.1016/j.bandl.2009.09.005

McCasland, J. S., & Konishi, M. (1981). Interaction between auditory and motor activities in an avian song control nucleus. *Proceedings of the National Academy of Sciences of the United States of America*, *78*(12), 7815–7819.

Mizrahi-Kliger, A. D., Kaplan, A., Israel, Z., & Bergman, H. (2018). Desynchronization of slow

oscillations in the basal ganglia during natural sleep. *Proceedings of the National Academy of Sciences of the United States of America*, *115*(18), E4274–E4283. https://doi.org/10.1073/pnas.1720795115

O'Keefe, J. (1976). Place units in the hippocampus of the freely moving rat. *Experimental Neurology*, *51*(1), 78–109.

Olveczky, B. P., Andalman, A. S., & Fee, M. S. (2005). Vocal experimentation in the juvenile songbird requires a basal ganglia circuit. *PLoS Biology*, *3*(5), e153. https://doi.org/10.1371/journal.pbio.0030153

Pachitariu, M., Steinmetz, N., Kadir, S., Carandini, M., & Kenneth D., H. (2016). Kilosort: Realtime spike-sorting for extracellular electrophysiology with hundreds of channels. *bioRxiv*. https://doi.org/10.1101/061481

Pearson, K. (1895). Note on Regression and Inheritance in the Case of Two Parents. *Proceedings of the Royal Society of London Series I*, *58*, 240–242.

Ramanathan, D. S., Gulati, T., & Ganguly, K. (2015). Sleep-Dependent Reactivation of Ensembles in Motor Cortex Promotes Skill Consolidation. *PLOS Biology*, *13*(9), e1002263. https://doi.org/10.1371/journal.pbio.1002263

Ricker, W. E. (1973). Linear Regressions in Fishery Research. *Journal of the Fisheries Research Board of Canada*, *30*(3), 409–434. https://doi.org/10.1139/f73-072

Roeser, A., Gadagkar, V., Das, A., Puzerey, P. A., Kardon, B., & Goldberg, J. H. (2023). Dopaminergic error signals retune to social feedback during courtship. *Nature*, *623*(7986), 375–380. https://doi.org/10.1038/s41586-023-06580-w

Santos, F. J., Oliveira, R. F., Jin, X., & Costa, R. M. (2015). Corticostriatal dynamics encode the refinement of specific behavioral variability during skill learning. *eLife*, *4*, e09423. https://doi.org/10.7554/eLife.09423

Scharff, C., & Nottebohm, F. N. (1991). A comparative study of the behavioral deficits following lesions of various parts of the zebra finch song system: Implications for vocal learning. *The Journal of Neuroscience : The Official Journal of the Society for Neuroscience*, *11*(9), 2896–2913.

Schneider, M., Broggini, A. C., Dann, B., Tzanou, A., Uran, C., Sheshadri, S., Scherberger, H., & Vinck, M. (2021). A mechanism for inter-areal coherence through communication based on connectivity and oscillatory power. *Neuron*, *109*(24), 4050-4067.e12. https://doi.org/10.1016/j.neuron.2021.09.037

Shank, S. S., & Margoliash, D. (2009). Sleep and sensorimotor integration during early vocal learning in a songbird. *Nature*, *458*(7234), 73–77. https://doi.org/10.1038/nature07615

Shein-Idelson, M., Ondracek, J. M., Liaw, H., Reiter, S., & Laurent, G. (2016). Slow waves, sharp waves, ripples, and REM in sleeping dragons. *Science (New York, N.Y.)*, *352*(6285), 590–595. https://doi.org/10.1126/science.aaf3621

Siapas, A. G., & Wilson, M. A. (1998). Coordinated interactions between hippocampal ripples and cortical spindles during slow-wave sleep. *Neuron*, *21*(5), 1123–1128.

Solis, M. M., Brainard, M. S., Hessler, N. A., & Doupe, A. J. (2000). Song selectivity and sensorimotor signals in vocal learning and production. *Proceedings of the National Academy of Sciences of the United States of America*, *97*(22), 11836–11842. https://doi.org/10.1073/pnas.97.22.11836

Tumer, E. C., & Brainard, M. S. (2007). Performance variability enables adaptive plasticity of “crystallized” adult birdsong. *Nature*, *450*(7173), 1240–1244. https://doi.org/10.1038/nature06390

Vates, G. E., & Nottebohm, F. (1995). Feedback circuitry within a song-learning pathway. *Proceedings of the National Academy of Sciences of the United States of America*, *92*(11), 5139–5143.

Vates, G. E., Vicario, D. S., & Nottebohm, F. (1997). Reafferent thalamo- “cortical” loops in the song system of oscine songbirds. *The Journal of Comparative Neurology*, *380*(2), 275–290.

Warren, T. L., Tumer, E. C., Charlesworth, J. D., & Brainard, M. S. (2011). Mechanisms and time course of vocal learning and consolidation in the adult songbird. *Journal of Neurophysiology*, *106*(4), 1806–1821. https://doi.org/10.1152/jn.00311.2011

Wise, S. P., Murray, E. A., & Gerfen, C. R. (1996). The frontal cortex-basal ganglia system in primates. *Critical Reviews in Neurobiology*, *10*(3–4), 317–356. https://doi.org/10.1615/critrevneurobiol.v10.i3-4.30

Wu, H. G., Miyamoto, Y. R., Castro, L. N. G., Ölveczky, B. P., & Smith, M. A. (2014). Temporal structure of motor variability is dynamically regulated and predicts motor learning ability. *Nature Neuroscience*, *17*(2), 312–321. https://doi.org/10.1038/nn.3616

Yanagihara, S. Y., & Hessler, N. A. (2012). Phasic basal ganglia activity associated with high-gamma oscillation during sleep in a songbird. *Journal of Neurophysiology*, *107*(1), 424–432. https://doi.org/10.1152/jn.00790.2011

Yeganegi, H., Luksch, H., & Ondracek, J. M. (2019). Hippocampal-like network dynamics underlie avian sharp wave-ripples. *bioRxiv*, 825075. https://doi.org/10.1101/825075

Yeganegi, H., & Ondracek, J. M. (2023). Multi-channel recordings reveal age-related differences in the sleep of juvenile and adult zebra finches. *Scientific Reports*, *13*(1), Article 1. https://doi.org/10.1038/s41598-023-35160-1

Yin, H. H., Mulcare, S. P., Hilário, M. R. F., Clouse, E., Holloway, T., Davis, M. I., Hansson, A. C., Lovinger, D. M., & Costa, R. M. (2009). Dynamic reorganization of striatal circuits during the acquisition and consolidation of a skill. *Nature Neuroscience*, *12*(3), Article 3. https://doi.org/10.1038/nn.2261

Young, B. K., Mindlin, G. B., Arneodo, E., & Goller, F. (2017). Adult zebra finches rehearse highly variable song patterns during sleep. *PeerJ*, *2017*(11), 1–18. https://doi.org/10.7717/peerj.4052

Zai, A. T., Cavé-Lopez, S., Rolland, M., Giret, N., & Hahnloser, R. H. R. (2020). Sensory substitution reveals a manipulation bias. *Nature Communications*, *11*(1), 5940. https://doi.org/10.1038/s41467-020-19686-w